# CENTROID SWINGING PROPERTY OF A MACHINE BODY UNDERGOING LONGITUDINAL EXCITATION IN A STRAW COMPRESSION BALER

## Zhong Tang[1*], Haoyang Wang[1], Tiantian Jing[1], Sifan Liu[1], Cheng Shen[2]

[1*]Corresponding author. School of Agricultural Engineering, Jiangsu University, Zhenjiang 212013, China.
E-mail: tangzhong2012@126.com | ORCID ID: https://orcid.org/0000-0002-2724-115X

**ABSTRACT**

During the harvesting of waste straw in the field, a self-propelled baler undergoes significant oscillations in the longitudinal direction around its centre of gravity, which greatly affect the stability of operation and the comfort of the driver. In order to analyse the vibration characteristics of the main frame under multi-source excitation, the complete frame is divided into a chassis frame and a baling frame. A nine-degree-of-freedom vibration system model of the whole machine is established based on the relationship between the internal motion devices, and simulations are carried out using MATLAB/Simulink. In addition, a multi-body dynamics simulation of the compression device is carried out, and the law governing the variation in force at different unit points of the mechanism is analysed. Finally, the vibration response of the main frame under different working conditions is explored. The results show that the main frequency component of the frame in the no-load state is 80 Hz, and the main response frequency of the frame is about 1.6 Hz, a finding that is consistent with the operating frequency of the compression mechanism. In particular, the displacement amplitude of the simulated signal at the centroid position is consistent with that measured in experiments, which verifies the validity of the dynamic model. Our results can provide guidance for future work aiming to further reduce the body vibration amplitude and optimise the design of the frame.

## INTRODUCTION

China has abundant crop straw resources, with an annual production of nearly 800 million tons. The use of self-propelled balers has enabled the development of an integrated recycling process for the picking, feeding and compression baling of field waste straw, which can effectively promote the large-scale and comprehensive utilisation of straw resources (Tang et al., 2020a; Guo et al., 2022; Yin et al., 2023). However, during the straw compression operation, the reciprocating motion of the crank slider has a strong impact on the whole machine, which causes the frame to undergo vibration with a large range of amplitudes in the longitudinal direction (Guerrieri et al., 2019; Zhao et al., 2018). It is therefore necessary to characterise the state of the frame during the straw compression process, so as to provide a

reference for finding an optimal control method to reduce the amplitude of the machine body (Xu et al., 2019; Ma et al., 2023; Pang et al., 2019).

Many scholars have conducted extensive research on the dynamic modelling and vibration reduction of straw compression balers. In order to improve the driving comfort of an agricultural tractor drawn by a large square baler, Langer et al. (2015) proposed a method of improving the vibration reduction of the seat from the perspective of ergonomics, in view of the phenomenon whereby the machine is exposed to multi-dimensional excitation over a long period. With a particular focus on exploring the vibration of the whole machine during the operation, Li et al. (2017) considered the problems of high vibration noise and low driving comfort of a combined harvest baling complex machine. Through testing,

it was found that the unbalanced rotary motion moment of the threshing drum and the fan, and the reciprocating motion of the vibrating screen and the compression device, were the main causes of vibration for the whole machine. In order to prevent fracture and excessive stress on the working parts caused by vibration, the finite element analysis method has also been widely applied to the optimisation of the frame and the design of key components of the baler (Bai et al., 2011; Song et al., 2014). In terms of both operational stability and component reliability, the impact of large-scale vibrations during the operation of the machine is negative (Liu et al., 2023; Wang et al., 2021). However, current measures have only improved some of the problems caused by vibration, and the obvious problem of swinging near the centroid position of the body, which is caused by the unbalanced inertial force of the compression device, persists (Wei et al., 2018; Yu et al., 2024). Existing research has focused on the characterisation of the inertial force of the slider-crank mechanism and corresponding vibration reduction measures. By changing the combination of the inertial acceleration, maximum principal stress and contact force of the mechanism, the friction of the mechanical system can be reduced, and the stability and service life can be improved (Albaghdadi et al., 2021; Wang et al., 2023). Etesami et al. (2019) considered the vibration force and vibration moment as the objective function, and carried out multi-objective optimisation in which the mass, moment of inertia, and centroid position of the mechanism connecting rod were used as design variables; this approach improved the dynamic balance of the crank-slider mechanism. In addition, some scholars (Tao & Wang, 2017) have developed vibration reduction methods for the mechanism through lightweight design. For example, Han & Ding (2023) aimed to reduce the mass of the slider and the equivalent inertial force, and carried out topology optimisation without affecting the strength and stiffness. These authors also established a single-degree-of-freedom vibration system model to provide a reference for the vibration reduction of the press machine.

The problem of vibration of a self-propelled baler has been widely considered, and several improvement measures have been put forward. However, a lack of relevant research on the characterisation of the longitudinal vibration state of the frame during the straw compression operation is an important limiting factor, and the law governing the changes in force of the mechanism during the process of straw compression is not yet fully understood. We therefore explore the amplitude characteristics of the frame under the influence of multi-source excitation force, and characterise these by establishing a nine-degree-of-freedom vibration system model. The characteristics of the dynamic force variation of the compression mechanism during straw compression are then analysed via a multi-body dynamics simulation. Vibration tests of the whole machine under different working conditions are then carried out, and the main frequency components of the fuselage and the amplitude characteristics of the frame are determined. The simulation results for the whole vibration system model are then compared with experimental results to verify the effectiveness of the model. Finally, the rule governing the periodic oscillations near the centroid position of the machine body induced by the straw compression process is determined.

## MATERIAL AND METHODS

### Structure and vibration system model of a straw compression baler

The frame of a straw compression baler is mainly formed of a chassis frame and a baling frame. As shown in Figure 1(a), the baling frame forms the basis for installation of the roller, the conveying fork, the compression mechanism and the transmission system. The chassis frame is connected to a tracked chassis to provide support for the whole machine (Tang et al., 2020b). During operation in the field, the whole machine can be regarded as a multi-degree-of-freedom linear elastic system, and the frame vibrates and deforms under the combined excitation force of multiple vibration sources.
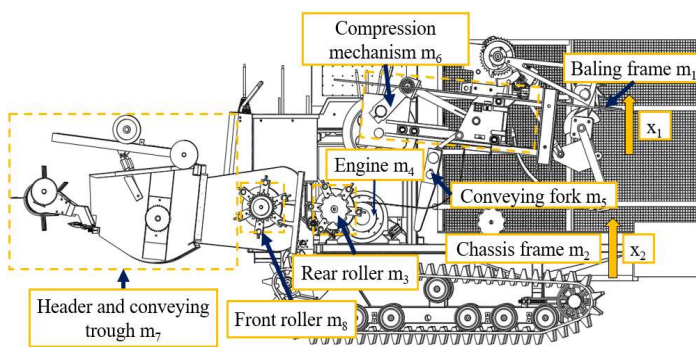


(a) Structure of a self-propelled baler
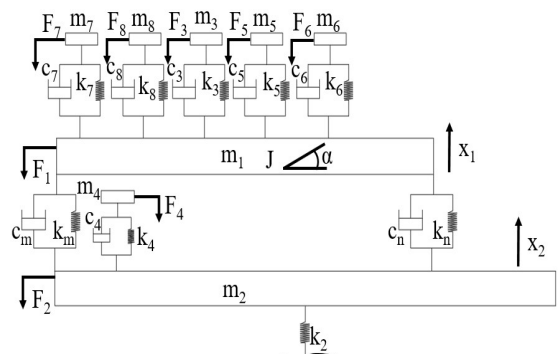
(b) Vibration model with nine degrees of freedom

FIGURE 1. Main structure and vibration system model of a self-propelled baler.

We neglected the horizontal excitation force exerted by the vibration source on the frame, and the vertical displacement $x_1$, $x_2$ and pitching angle $\alpha$ of the frame around its transverse horizontal centroid axis were taken as generalised coordinates for the model. Figure 1(b) shows the vibration system model of the whole machine. The key moving parts were discretised and simplified as several rigid components connected by springs and dampers. The actual masses of both the frame and the key moving parts were

determined through weighing experiments. Furthermore, the chassis frame and tracked chassis were regarded as rigid connections. The damping force and spring force were assumed to be linear functions of the velocity and displacement, respectively, and the coefficients represent their vectors.

The frame is formed by welding hollow steel components with a rectangular cross-section. A schematic diagram of the cross-section is shown in Figure 2. Each working device is firmly attached at the centre of the frame,

and we assume it to be a fixed beam with a uniformly distributed mass at both ends. It is also assumed that the mass of the beam is negligible, and the external mass is concentrated at its midpoint. Based on actual measurements, the length of the rectangular hollow section is taken as 0.5 m, and the width $b$ and height $h$ are 38 mm and 48 mm, respectively.
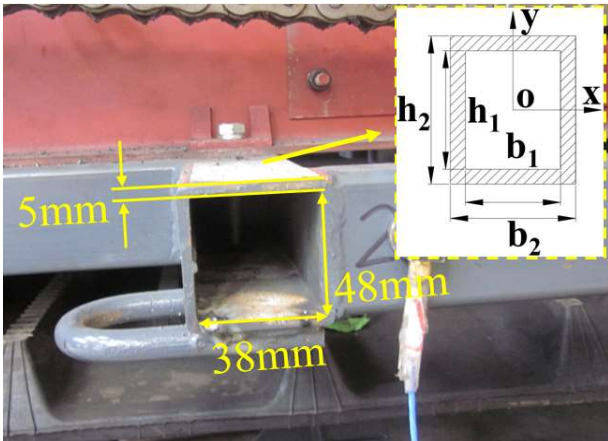


(a) Section of a square tube used for the frame
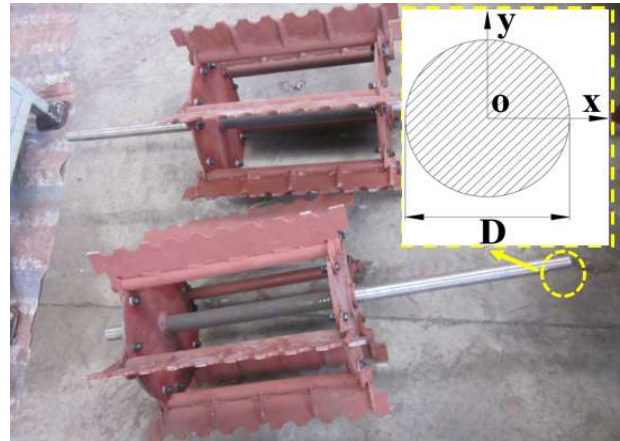


(b) Section of the round roller drive shaft

FIGURE 2. Cross-section diagrams.

The equivalent spring stiffness of the simplified frame, the moment of inertia for the rectangular square tube section, the moment of inertia for the circular section, the stiffness of the shaft end, and the damping coefficient obtained based on the loss coefficient are calculated as follows:

$$k_{eq} = \frac{48EI}{L^3} \times 4 \tag{1}$$

$$I_1 = \frac{1}{12}(b_2 h_2{}^3 - b_1 h_1{}^3) \tag{2}$$

$$I_2 = \frac{\pi D^4}{64} \tag{3}$$

$$K = \frac{GJ_{p0}}{L} \tag{4}$$

$$C_{ij} = \frac{\psi K_{ij}}{2\pi\omega} \tag{5}$$

Where:

$I$ is the moment of inertia of the cross section;

$L$ is the length of the shaft section;

$D$ is the diameter of the circular section;

$J_{p0}$ is the polar moment of inertia of the section; and the moment of inertia $J$ of the baling frame around the lateral axis is taken as 1200 kg·m².

Since most of the frame components are made from Q235 structural steel, the elastic modulus E is set to $2.1 \times 10^{11}$ N·m$^{-2}$ and the shear modulus G to $8 \times 10^{10}$ N·m$^{-2}$. The value of $L$ for the roller is 0.95 m, and the diameter $D$ of the circular section is 0.03 m; the value of $L$ for the conveying fork is 0.7 m, and the diameter $D$ of the circular section is 0.06 m; the value of $L$ of the compression device is 0.45 m, and the diameter $D$ of the circular section is taken as 0.098 m; and the value of $L$ for the square-section tube of the frame is taken as 0.5 m. Finally, the parameters required for the simulation model, obtained from calculation and statistics, are shown in Table 1.

TABLE 1. List of simulation parameters.

| Parameter | Value | Parameter | Value |
|---|---|---|---|
| Mass of the baling frame $m_1$ | 360 kg | Mass of the chassis frame $m_2$ | 416 kg |
| Mass of the rear roller $m_3$ | 52 kg | Mass of the engine $m_4$ | 150 kg |
| Mass of the conveying fork $m_5$ | 138 kg | Mass of the compression device $m_6$ | 125 kg |
| Mass of the header and conveyor trough $m_7$ | 340 kg | Mass of the front roller $m_8$ | 52 kg |
| Vertical stiffness of the baling frame $k_m$, $k_n$ | $5.91 \times 10^7$ N/m | Vertical damping of the baling frame $c_m$, $c_n$ | 250 N·s/m |
| Vertical stiffness of the chassis frame $k_2$ | $5.91 \times 10^7$ N/m | Vertical damping of the chassis frame $c_2$ | 0 N·s/m |
| Vertical stiffness of the engine $k_4$ | $6 \times 10^3$ N/m | Vertical damping of the engine $c_4$ | 225 N·s/m |
| Vertical stiffness of the header and trough $k_7$ | $5.5 \times 10^3$ N/m | Vertical damping of the header and trough $c_7$ | 300 N·s/m |
| Vertical stiffness of the front roller $k_8$ | $3.35 \times 10^3$ N/m | Vertical damping of the front roller $c_8$ | 175 N·s/m |
| Vertical stiffness of the rear roller $k_3$ | $3.35 \times 10^3$ N/m | Vertical damping of the rear roller $c_3$ | 175 N·s/m |
| Vertical stiffness of the conveying fork $k_5$ | $7.27 \times 10^4$ N/m | Vertical damping of the conveying fork $c_5$ | 350 N·s/m |
| Vertical stiffness of the compression device $k_6$ | $8.05 \times 10^5$ N/m | Vertical damping of the compression device $c_6$ | 400 N·s/m |
| Distance from the engine to the centre of mass $l_4$ | 0.4 m | Distance from the drive shaft of the trough to the centre of mass $l_7$ | 0.55 m |
| Distance from the drive shaft of the front roller to the centre of mass $l_8$ | 0.75 m | Distance from the drive shaft of the rear roller to the centre of mass $l_3$ | 0.5 m |
| Distance from the drive shaft of the conveying fork to the centre of mass $l_5$ | 0.15 m | Distance from the drive shaft of the compression mechanism to the centre of mass $l_6$ | 0.2 m |
| Distance between the front of the baling frame and the centre of mass $l_m$ | 0.6 m | Distance between the rear side of the baling frame and the centre of mass $l_n$ | 0.4 m |

The differential equations for the nine-degree-of-freedom system are established based on Newton's second law of motion. When studying the vertical and pitching motion of the frame, the spring coefficients and damping coefficients of the front and rear supports can be replaced by the equivalent spring coefficients $k_m$ and $k_n$ and equivalent damping coefficients $c_m$ and $c_n$, respectively. We assume that there is a vertical upward displacement $x_2$ at the position of the centre of mass of the chassis frame and a vertical upward displacement $x_1$ at the centroid position of the baling frame, and the vibration differential equation is established and arranged as a matrix as follows:

$$M\ddot{x}(t) + C\dot{x}(t) + Kx(t) = f(t) \qquad (6)$$

Where:

$M$ is the mass matrix, $C$ is the damping coefficient matrix, and $K$ is the stiffness coefficient matrix;

$$x = \left[ x_1, x_2, \alpha, x_3, x_4, x_5, x_6, x_7, x_8 \right]^T;$$

$$M = \begin{bmatrix} m_1 & 0 & 0 & 0 & 0 & 0 & 0 & 0 & 0 \\ 0 & m_2 & 0 & 0 & 0 & 0 & 0 & 0 & 0 \\ 0 & 0 & J & 0 & 0 & 0 & 0 & 0 & 0 \\ 0 & 0 & 0 & m_3 & 0 & 0 & 0 & 0 & 0 \\ 0 & 0 & 0 & 0 & m_4 & 0 & 0 & 0 & 0 \\ 0 & 0 & 0 & 0 & 0 & m_5 & 0 & 0 & 0 \\ 0 & 0 & 0 & 0 & 0 & 0 & m_6 & 0 & 0 \\ 0 & 0 & 0 & 0 & 0 & 0 & 0 & m_7 & 0 \\ 0 & 0 & 0 & 0 & 0 & 0 & 0 & 0 & m_8 \end{bmatrix}; C = \begin{bmatrix} C_{11} & -(c_m+c_n) & C_{13} & -c_3 & 0 & -c_5 & -c_6 & -c_7 & -c_8 \\ -(c_m+c_n) & (c_4+c_m+c_n) & c_m l_m - c_n l_n & 0 & -c_4 & 0 & 0 & 0 & 0 \\ C_{31} & c_m l_m - c_n l_n & C_{33} & c_3 l_3 & 0 & -c_5 l_5 & -c_6 l_6 & c_7 l_7 & c_8 l_8 \\ -c_3 & 0 & c_3 l_3 & c_3 & 0 & 0 & 0 & 0 & 0 \\ 0 & -c_4 & 0 & 0 & c_4 & 0 & 0 & 0 & 0 \\ -c_5 & 0 & -c_5 l_5 & 0 & 0 & c_5 & 0 & 0 & 0 \\ -c_6 & 0 & -c_6 l_6 & 0 & 0 & 0 & c_6 & 0 & 0 \\ -c_7 & 0 & c_7 l_7 & 0 & 0 & 0 & 0 & c_7 & 0 \\ -c_8 & 0 & c_8 l_8 & 0 & 0 & 0 & 0 & 0 & c_8 \end{bmatrix}$$

$$C_{11} = c_m + c_n + c_7 + c_8 + c_3 + c_5 + c_6;$$

$$C_{13} = C_{31} = -(c_m l_m - c_n l_n + c_7 l_7 + c_8 l_8 + c_3 l_3 - c_5 l_5 - c_6 l_6);$$

$$C_{33} = c_m l_m^2 + c_n l_n^2 + c_7 l_7^2 + c_8 l_8^2 + c_3 l_3^2 + c_5 l_5^2 + c_6 l_6^2 ;$$

$$K = \begin{bmatrix} K_{11} & -(k_m + k_n) & K_{13} & -k_3 & 0 & -k_5 & -k_6 & -k_7 & -k_8 \\ -(k_m + k_n) & (k_4 + k_m + k_n + k_2) & k_m l_m - k_n l_n & 0 & -k_4 & 0 & 0 & 0 & 0 \\ K_{31} & k_m l_m - k_n l_n & K_{33} & k_3 l_3 & 0 & -k_5 l_5 & -k_6 l_6 & k_7 l_7 & k_8 l_8 \\ -k_3 & 0 & k_3 l_3 & k_3 & 0 & 0 & 0 & 0 & 0 \\ 0 & -k_4 & 0 & 0 & k_4 & 0 & 0 & 0 & 0 \\ -k_5 & 0 & -k_5 l_5 & 0 & 0 & k_5 & 0 & 0 & 0 \\ -k_6 & 0 & -k_6 l_6 & 0 & 0 & 0 & k_6 & 0 & 0 \\ -k_7 & 0 & k_7 l_7 & 0 & 0 & 0 & 0 & k_7 & 0 \\ -k_8 & 0 & k_8 l_8 & 0 & 0 & 0 & 0 & 0 & k_8 \end{bmatrix},$$

$$K_{11} = k_m + k_n + k_7 + k_8 + k_3 + k_5 + k_6 ;$$

$$K_{13} = K_{31} = -(k_m l_m - k_n l_n + k_7 l_7 + k_8 l_8 + k_3 l_3 - k_5 l_5 - k_6 l_6) ;$$

$$K_{33} = k_m l_m^2 + k_n l_n^2 + k_7 l_7^2 + k_8 l_8^2 + k_3 l_3^2 + k_5 l_5^2 + k_6 l_6^2 ;$$

$$f(t) = \begin{bmatrix} 0 & 0 & 0 & f_3(t) & f_4(t) & f_5(t) & f_6(t) & f_7(t) & f_8(t) \end{bmatrix}^T ;$$

Where:

$m_i$ is the mass of each key component (kg);

$x_i$ is the vertical displacement variable (m);

$\dot{x}_i$ is the vertical velocity variable (m·s$^{-1}$);

$\ddot{x}_i$ is the vertical acceleration variable (m·s$^{-2}$);

$k_i$ is the damping coefficient (N·m$^{-1}$);

$c_i$ is the vertical damping coefficient (N·m$^{-1}$);

$J$ is the moment of inertia of the baling frame around the lateral axis (kg·m$^2$);

$\alpha$ is the pitch angle displacement variable of the baling frame (rad);

$l_i$ is the longitudinal distance between the centroid position of each rotating axis or component and the centroid position of the baling frame, and

$l_m$ and $l_n$ are the longitudinal distances between the two sides of the baling frame and the centroid position, respectively (m).

It can also be seen that the non-diagonal elements of matrix $K$ and $C$ are not zero, whereas the non-diagonal elements of the mass matrix $M$ are all zero, which indicates that the degrees of freedom of the key components in the system are interrelated. In addition, in order to obtain the transfer function matrix of the system, the differential equation of the whole-machine vibration model in matrix form was subjected to a Laplace transform, giving the following expression:

$$Ms^2 + Cs + Kx(s) = f(s) \tag{7}$$

If $B(s)=(Ms^2+Cs+K)$, the formula above is transformed into:

$$x(s) = B(s)^{-1} f(s) = \frac{adjB(s)}{detB(s)} f(s) = Hf(s) \tag{8}$$

Where:

$H$ is the transfer function matrix of the dynamic vibration model of whole machine:

$$H(s) = B(s)^{-1} = \frac{adjB(s)}{detB(s)} \tag{9}$$

**Multi-body dynamics simulation of the compression mechanism**

**Reciprocating motion model of the compression mechanism**

The straw compression device can be treated as a crank connecting rod mechanism, which drives the piston back and forth between points $C_1$ and $C_2$ along the operating track via the connecting rod. The movement section of the piston coincides with the section of the track beam, as shown in Figures 3 and 4. When the piston moves to point $C_1$, the body of the machine will tilt forward with support point F, due to the change in the inertial force of the mechanism. Similarly, when the piston moves to point $C_2$, it will tilt backward with support point R.
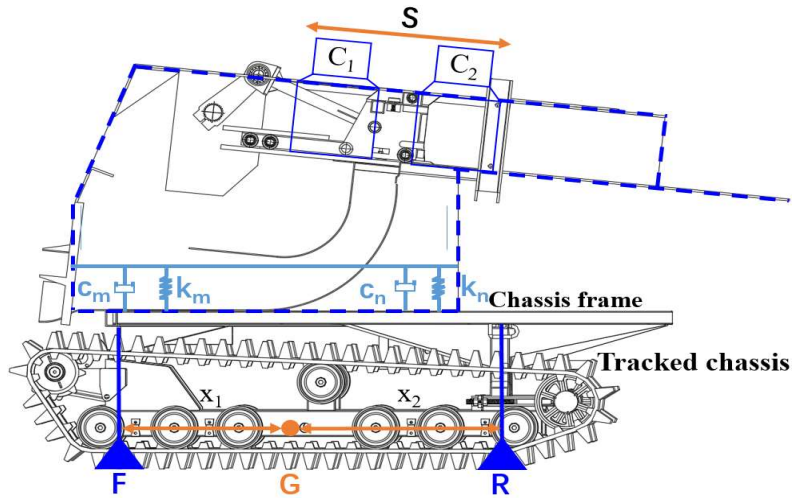
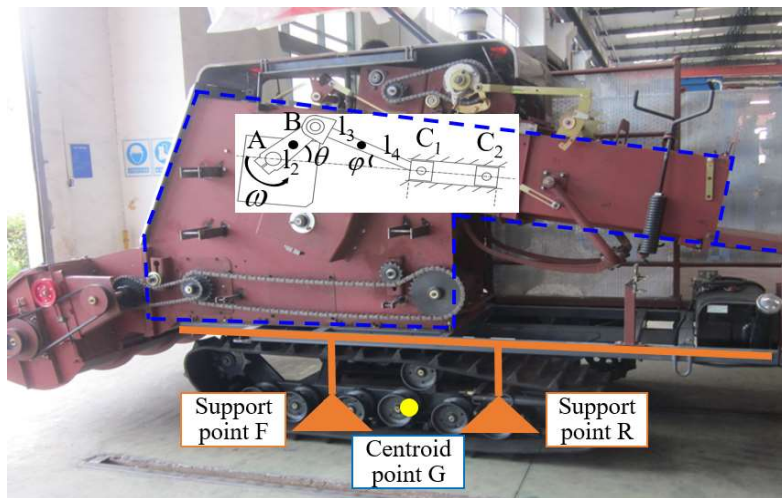FIGURE 3. Schematic diagram showing the movement of the mechanism.



FIGURE 4. Diagram showing the physical support points.

In this study, the mass substitution method is used to equivalently substitute the mass of the crank and connecting rod to three rotation centres. The equivalent mass at point A does not generate inertial force, and the unbalanced mass at point B includes part of the mass of the crank and connecting rod. The concentrated mass at point C includes the mass of the piston and part of the mass of the connecting rod. The substitution equations are as follows:

$$\begin{cases} m_b = \dfrac{l_4}{l} \cdot m_3 + \dfrac{l_2}{r} \cdot m_2 \\ m_c = \dfrac{l_3}{l} \cdot m_3 + m_4 \end{cases} \quad (10)$$

Where:

$r$ and $l$ are the lengths of the crank and connecting rod, respectively;

$m_2$, $m_3$ and $m_4$ are the masses of the crank, connecting rod and piston, respectively, and

$l_2$, $l_3$ and $l_4$ are the distances between point A and the crank centroid, point B and the connecting rod centroid, and point C and the connecting rod centroid, respectively.

The equations for the displacement and acceleration of the piston are:

$$\begin{cases} s = r\cos\theta + l \cdot \cos\varphi \\ a_c = -\omega^2 r\cos\theta + \omega^2 \dfrac{r^2\left[l^2\left(1-2\cos^2\theta\right)-r^2\sin^4\theta\right]}{\left[l^2-\left(r\sin\theta\right)^2\right]^{\frac{3}{2}}} \end{cases} \quad (11)$$

Where:

$\theta$ is the angle through which the crank rotates counterclockwise,

$\varphi$ is the angle between the connecting rod and the track, and $\lambda$ is the ratio of $r$ to $l$.

By expanding [eq. (11)] using a Taylor series, we obtain the expression:

$$\cos\varphi = \sqrt{1-\lambda^2\sin^2\theta} = 1-\frac{1}{2}\left(\lambda^2\sin^2\theta\right)-\frac{1}{8}\left(\lambda^4\sin^4\theta\right)-\frac{1}{16}\left(\lambda^6\sin^6\theta\right)-L \tag{12}$$

Since the ratio is very small, [eq. (11)] can be simplified as follows, ignoring the higher-order terms:

$$s = r\cos\theta + l\cdot\left(1-\frac{1}{2}\lambda^2\sin^2\theta\right) \tag{13}$$

$$a_c = -\omega^2 r\left(\cos\theta + \lambda\cos 2\theta\right) \tag{14}$$

Hence, the reciprocating inertial force of the piston during linear motion is:

$$F_C = -m_c a_c = -m_c\omega^2 r\left(\cos\theta + \lambda\cos 2\theta\right) \tag{15}$$

The rotational inertial force of the equivalent mass at point B can be expressed as:

$$F_B = -m_b v_b = -m_b\omega^2 r \tag{16}$$

The total inertial force of the mechanism in the direction of movement of the piston is composed of the component of the rotational inertial force of the mass at point B in this direction and the reciprocating inertial force of the piston. The expression for this force is shown in [eq. (17)]:

$$F_X = F_{Bx} + F_C = -m_b\omega^2 r\cos\theta - m_c\omega^2 r\left(\cos\theta + \lambda\cos 2\theta\right) \tag{17}$$

Through a static analysis of the compression device, it can be concluded that the rotating centrifugal inertial force at point B and the reciprocating inertial force at point C of the mechanism are both proportional to the square of the crank speed. Hence, the magnitude of the inertia force cannot be ignored during the straw compression process, and there is obvious swinging near the centroid position of the machine body as a result.
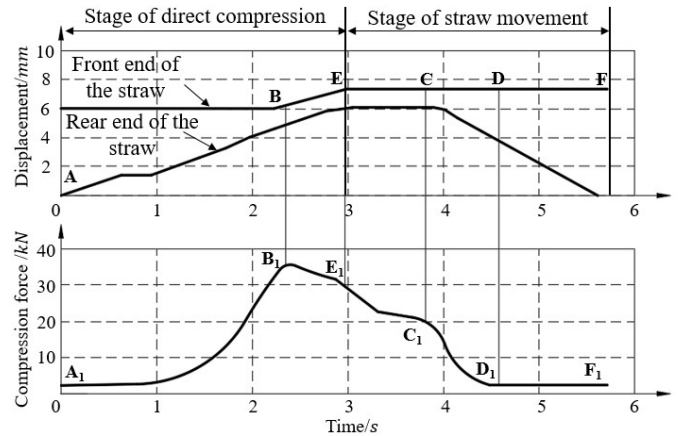
**Simulation fitting modelling of straw compression characteristics**

In order to add reasonable loads to the simulation model, the mechanical characteristics of straw during compression were analysed and mathematical models at different stages were fitted (Khawaja & Khan, 2022; Zhang & Peng, 2018). The compression mechanism adopted in this paper is based on an open compression method, with a compression frequency of 96.5 r·m$^{-1}$ and a feed rate of 3 kg·s$^{-1}$. The power is transmitted from the flywheel to the gearbox transmission shaft, which then drives the crank to rotate at a constant speed. Finally, the straw is continuously compressed through the reciprocating motion of the piston, until it forms a bundle. The operational process and the work done by the piston during compression are shown in Figure 5.
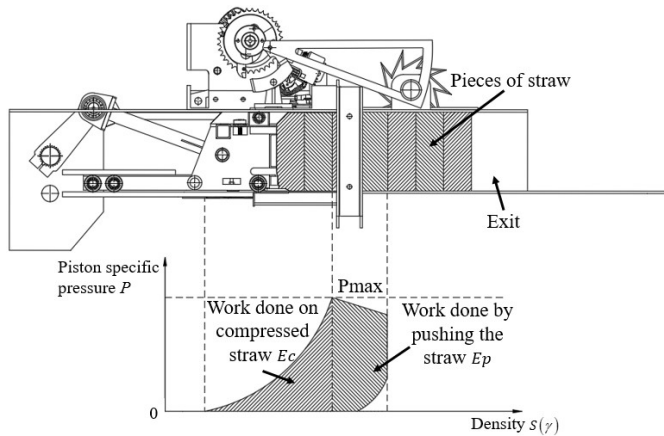


(a) Schematic diagram showing the open compression structure     (b) Compression force and displacement of the piston

FIGURE 5. Compression process for the straw

During the compression process of the straw, the compression force undergoes a nonlinear change with time. As shown in Figure 5(b), this process can be divided into three stages according to the changes in the compression force. The first stage, $A_1B_1$, involves compression of the straw; in this stage, the compression force and the displacement have an exponential relationship, and the deformation mainly involves eliminating the gaps between pieces of straw. The compression force quickly increases to reach a maximum. The second stage, $B_1C_1$, involves stress relaxation, in which the compressive force decreases with time. The third stage, $C_1D_1$, involves straw rebounding, and the changes at this stage are similar to the curve for the first stage, $A_1B_1$, although the variable coefficients are different. The corresponding mechanical mathematical model was therefore fitted by comprehensively considering the deformation characteristics of the straw compression process, and the curve was simulated by means of simulating a spring using ADAMS software. The corresponding mathematical model for the simulation is shown in [eq. (18)]:

$$F = -k(r - r_0) - c\frac{dr}{dt} + f_0 \qquad (18)$$

Where:

$k$ and $c$ are the stiffness coefficient and damping coefficient of the simulated spring respectively;

$r$ and $r_0$ are the length and initial length of the simulated spring respectively;

$\dfrac{dr}{dt}$ is the deformation velocity of the simulated spring;

$f_0$ is the preload force of the simulated spring.

In the compression stage $A_1B_1$ and the rebound stage $C_1D_1$, the changes in the compression force with time are similar. Hence, the same mathematical model can be used for fitting, except that the variable coefficients are different. Finally, the equation for the straw deformation process in these two stages is as follows after logarithmic fitting:

$$Y = \ln y = \ln Ae^{Br} = \ln A + Br = \ln A + B(r - r_0) \quad (19)$$

Where:

$r$ is the compression displacement of the simulated spring.

In the stress relaxation stage, $B_1C_1$, the type of friction between the straw and the compression chamber changes from static to dynamic, and the deformation of the straw is small. Due to the short period of time involved, the compression force and time can be directly modelled as a linear relationship. The fitting equation for the simplified mathematical model is as follows:

$$y = Mt + N \qquad (20)$$

Where:

$t$ is the simulation time for the straw compression process.

According to existing theories about the viscoelastic characteristics of fresh straw during the compression process (Tang et al., 2023; Shi et al., 2023; El-Sayed & Elsaid Mohamed, 2018), the parameters of the simulated spring and the fitted mathematical model in the simulation can be calculated as follows: direct compression stage: $k = 17.33$ N·mm⁻¹, $c = 2.23$ N·s·mm⁻¹; stress relaxation stage: $M = 14828.78$, $N = -7321.33$; straw rebound stage: $k = 16.91$ N·mm⁻¹, $c = 9.82$ N·s·mm⁻¹.

**Parameter settings and constraints for the simulation model**

In this study, SolidWorks was used to establish a three-dimensional structure diagram of the sub-parts in equal proportions, which was then imported into ADAMS for processing. The axis of the transmission shaft of the compression mechanism was set as the Z-direction of the model, the gravity of the mechanism as the Y-direction, and the direction of movement of the slider as the X-direction. Accurate setting of the coordinate directions is conductive to the simulation and positioning of the ADAMS model.
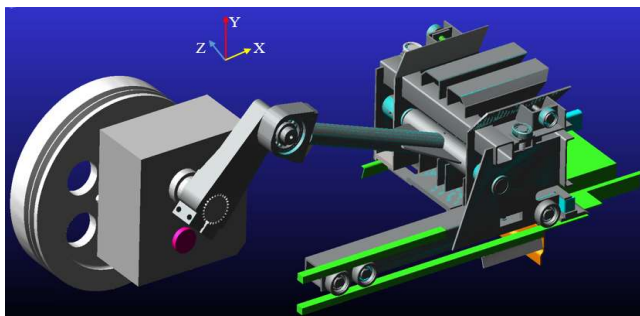


(a) Isometric view
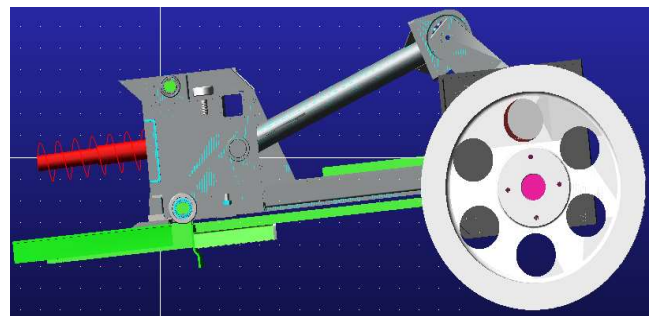


(b) Addition of load

FIGURE 6. Simulation settings in ADAMS.

Next, the working environment was set for the simulation software. The default Cartesian coordinate system of the software was used to set the direction, and the MMKS standard unit system was selected. The direction of gravitational acceleration was determined, and the amplitude was set to 9806.65 mm·s⁻². Since the dynamic modelling analysis presented in this paper only considers the mass, the moment of inertia and the movement of the centroid position of mechanism, the material of the compression mechanism was selected as steel. When the material properties of each part in the model had been set, the software was used to automatically calculate the relevant parameters for each part.

The parts that could be combined and which did not affect the movement of the mechanism were merged to form one body through Boolean operations. Next, in order to distinguish the merged parts, the newly created part was set to different names and colours in ADAMS. Finally, constraints were added to the components: the crank and frame, the crank and connecting rod, and the connecting rod and piston were set to rotating pairs; the frame and the ground were set to a fixed pair; and the compression piston and the frame were set to a sliding pair. A diagram of the model after these settings is shown in Figure 6(b).

**Vibration test of the frame under different working conditions**

**Test conditions and distribution of measuring points**

In order to better adapt to the operating characteristics of the straw compression baler, we used 1A312E type three-dimensional acceleration sensors (MTS Systems, Depew, New York, USA) in this test to collect time-varying vibration signals. The signals were received and recorded with a DH5902N signal acquisition analyser (Donghua Testing Technology Co., Ltd. Jingjiang City, Jiangsu Province, China). The sensor used in this test had its own amplifier circuit, and the signal acquisition instrument had its own low-pass anti-aliasing filter. During the test, a continuous sampling process was adopted, and a reasonable sampling frequency of 2 kHz was set for the signal acquisition instrument according to the sampling theorem. The parameters for the equipment are shown in Table 2.

TABLE 2. Parameters for the test instruments and sensors.

| Equipment | Performance index | Parameter value |
|---|---|---|
| Three-direction acceleration sensor 1A312E | Range | ±500g |
| | Frequency response | 0.5~10 kHz |
| | Sensitivity | 100 mV*g⁻¹ |
| | Lateral sensitivity | <5% |
| Dynamic signal acquisition instrument DH5902N | Channel | 32 |
| | Sampling frequency | 256 kHz |
| | Distortion factor | <0.5% |
| | Signal input method | IEPE |

During the actual operation, the driver adjusts the accelerator over time to control the forward speed according to the different working conditions. This means that the speeds of the engine and the key working parts are different. This test was divided into two parts, as shown in Figures 7 and 8. A study of the idle speed conditions is very important for the research into the vibration of the whole machine, and this test therefore mainly involved an analysis of the vibration response characteristics of the frame under the idle speed of the throttle and the working state of the whole machine.
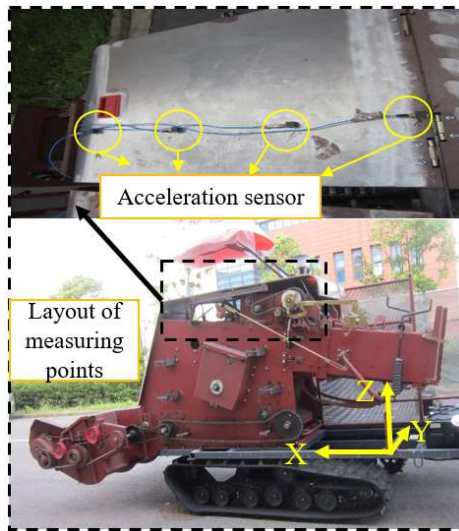


FIGURE 7. Indoor test conditions.

FIGURE 8. Outdoor test conditions.

In order to facilitate the subsequent data processing and analysis, a Cartesian coordinate system was established. The forward direction of the driver's seat was taken as the positive X-axis for the sensor, the left-hand side of the seat as the positive Y-axis, and the vertical direction from the ground as the positive Z-axis. The working conditions of the test and the status of the baler are shown in Table 3.

TABLE 3. Operating conditions of the straw compression baler in the test.

| Test scenario | Status of the straw compression baler | Test environment | Driving speed, km·h$^{-1}$ |
|---|---|---|---|
| 1 | Static, no load (engine only) | Indoor | 0 |
| 2 | Static, no load (all parts working) | Indoor | 0 |
| 3 | Moving state (engine only) | Outdoor | 10 |
| 4 | Moving state (all parts working) | Outdoor | 10 |

In this test, a total of 12 measuring points were selected for the key moving parts and the structural characteristic points of the frame, and the triaxial acceleration sensor was arranged to obtain the vibration signal. In particular, the excitation signal of the engine was collected by a sensor arranged at the transition point of the frame between the output shaft and the flywheel. The location of each measuring point is shown in Table 4.

TABLE 4. Locations of vibration measurement points.

| Measuring point | Location | Measuring point | Location |
|---|---|---|---|
| 1 | Transition frame for engine output shaft | 2 | Bearing housing for pickup drive shaft |
| 3 | Upper end of front roller shaft | 4 | Upper end of rear roller shaft |
| 5 | Bearing housing for the drive shaft of the conveying fork | 6 | Bearing housing for drive shaft of compression mechanism |
| 7 | Left front of chassis frame | 8 | Left rear of chassis frame |
| 9 | Right front of hay box | 10 | Rear right of hay box |
| 11 | Support for driver's seat | 12 | Bottom plate of the driver's platform |

**Time-frequency domain analysis of signals**

In this study, the vibration signals at each measuring point were analysed. The RMS values of the acceleration and the peak-to-peak values of displacement obtained by quadratic integration in three directions under different setting conditions were calculated as shown in [eq. (21)].

$$a_{rms} = \sqrt{\frac{1}{N}\sum_{i=1}^{N} a_i^2} = \sqrt{\frac{a_1^2 + a_2^2 + \cdots + a_N^2}{N}} \quad (21)$$

Where:

$a_i$ is the RMS value of acceleration in frequency band $i$ (m·s$^{-2}$);

$a_{rms}$ is the RMS value of acceleration in a single direction (m·s$^{-2}$), and

$N$ is the total number of frequency bands.

During normal harvesting operations in the field, the engine of the self-propelled baler should be run at the rated speed (2400 r·min$^{-1}$) to ensure good performance and efficiency. In this paper, a non-contact tachometer was used to measure the speed of each working part, and the theoretical excitation frequency was obtained through calculation, using [eq. (22)]. The results are shown in Table 5.

$$f = \frac{n}{60} \quad (22)$$

Where:

$f$ is the theoretical excitation frequency (Hz), and

$n$ is the rotation speed of the drive shaft of the moving part (r·min$^{-1}$).

TABLE 5. Main vibration source parameters.

| Vibration source | Rotating speed /rpm | Frequency /Hz | Vibration source | Rotating speed /rpm | Frequency /Hz |
|---|---|---|---|---|---|
| Engine | 2400 | 40 | Gear transmission | 391.7 | 6.53 |
| Engine drive shaft | 1354 | 22.57 | Rear roller | 569.8 | 9.50 |
| Knotted shaft | 96.5 | 1.61 | Front roller | 341.8 | 5.70 |
| Compression mechanism shaft | 96.5 | 1.61 | Picking up device | 141 | 2.35 |
| Transport bale shaft | 193 | 3.22 | Feeding auger | 226 | 3.77 |

It can therefore be calculated that the theoretical rotational excitation frequency of the diesel engine is 40 Hz, and the excitation frequency caused by combustion and inertial forces is 80 Hz. The frequency spectrum characteristics of the engine under these working conditions were obtained by a fast Fourier transform (FFT) of the vibration time-domain signal at measuring point 1 in the X direction, as shown in Figure 9.
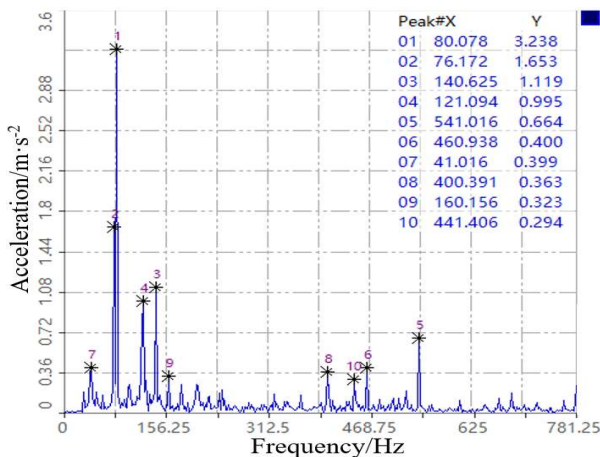


(a) Frequency corresponding to the first 10 peaks
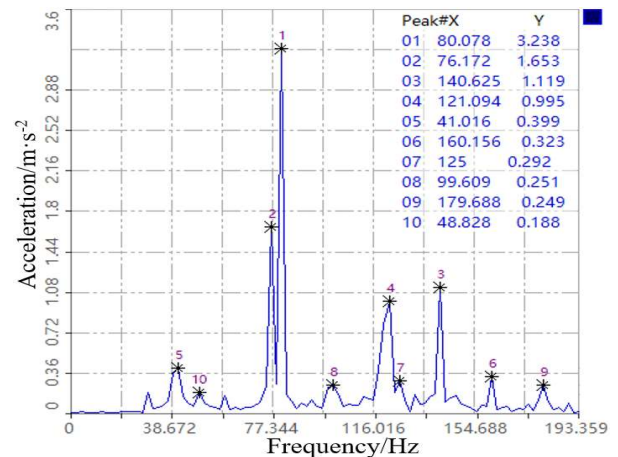


(b) Amplified graph of the low-frequency band

FIGURE 9. Spectrum maps for the engine under condition 1 (X-direction).

It can be seen from Figure 9 that the peak value of the vibration acceleration in the X-direction is the largest at a frequency of 80.078 Hz, which is the main frequency of engine vibration under the idling condition. It is also found that there is a multiplier component of 160.156 Hz, which verifies the accuracy of the test.

**RESULTS AND DISCUSSION**

**Vibration response of the machine body**

The data obtained from the calculations are shown in Table 6. In test condition 1, the diesel engine is the only excitation source, and its vibration intensity in all three directions is relatively large. The effective value of the vibration signal in the Z-direction at response points 11 and 12 of the cab is significantly greater than in other directions. This indicates that the vertical vibration at the driver's position is severe under this operating condition, resulting in a low level of comfort. The vibration response of the other measuring points is also continuously weakened during transmission.

TABLE 6. Time domain comparison of vibration intensity under various working conditions.

| Number | Effective value of vibration acceleration ($a_{rms}$, m·s$^{-2}$) and peak-to-peak displacement ($x_{pp}$, mm) | | | | | | | | | | | |
| --- | --- | --- | --- | --- | --- | --- | --- | --- | --- | --- | --- | --- |
| | Test condition 1 | | | | | | Test condition 2 | | | | | |
| | X | | Y | | Z | | X | | Y | | Z | |
| | $a_{rms}$ | $x_{pp}$ | $a_{rms}$ | $x_{pp}$ | $a_{rms}$ | $x_{pp}$ | $a_{rms}$ | $x_{pp}$ | $a_{rms}$ | $x_{pp}$ | $a_{rms}$ | $x_{pp}$ |
| 1 | 3.135 | 0.633 | 2.827 | 0.826 | 2.261 | 0.432 | 7.682 | 16.951 | 8.319 | 9.071 | 4.455 | 3.816 |
| 2 | 0.538 | 0.102 | 0.429 | 0.285 | 0.491 | 0.292 | 8.768 | 31.510 | 13.700 | 44.104 | 9.833 | 51.074 |
| 3 | 0.611 | 0.193 | 1.162 | 0.278 | 0.970 | 0.400 | 5.508 | 24.563 | 2.209 | 6.987 | 5.718 | 13.209 |
| 4 | 0.759 | 0.117 | 3.906 | 0.256 | 0.604 | 0.085 | 8.203 | 19.314 | 6.745 | 14.396 | 10.107 | 26.858 |
| 5 | 0.782 | 0.182 | 1.193 | 0.555 | 1.458 | 0.166 | 7.940 | 34.173 | 11.730 | 13.155 | 9.347 | 21.449 |
| 6 | 0.266 | 0.087 | 1.188 | 0.165 | 0.429 | 0.146 | 5.181 | 34.826 | 3.985 | 17.537 | 5.375 | 2.900 |
| 7 | 0.703 | 0.103 | 1.434 | 0.135 | 2.085 | 0.134 | 3.850 | 24.068 | 4.664 | 3.064 | 10.469 | 13.776 |
| 8 | 0.842 | 0.085 | 1.162 | 0.659 | 1.995 | 0.744 | 5.736 | 24.771 | 3.187 | 12.515 | 7.287 | 27.886 |
| 9 | 1.031 | 0.594 | 0.683 | 0.320 | 1.064 | 0.490 | 1.586 | 14.313 | 1.386 | 6.085 | 2.977 | 17.941 |
| 10 | 0.974 | 0.513 | 0.798 | 0.409 | 1.112 | 0.478 | 1.759 | 12.444 | 1.539 | 15.970 | 3.030 | 46.002 |
| 11 | 2.464 | 0.190 | 3.372 | 0.384 | 7.104 | 1.191 | 2.888 | 15.037 | 3.655 | 3.107 | 8.296 | 3.483 |
| 12 | 2.341 | 0.247 | 3.942 | 0.337 | 7.981 | 0.744 | 4.702 | 19.595 | 5.269 | 5.031 | 14.044 | 15.028 |

In test condition 2, the whole machine is in a working state, and the effective values of vibration acceleration in all three directions at each measuring point increase significantly. From the statistical data, it can be found that the RMS value of the vibration acceleration in the X-direction and the Z- direction at each measurement point at the excitation source position is strong, and the maximum peak-to-peak value of the displacement calculated by the acceleration signal is in these two directions, indicating that there is a large range of vibration in the longitudinal direction.
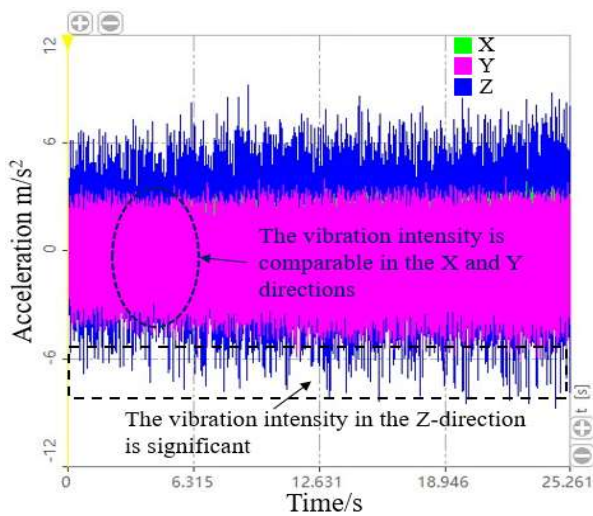


(a) Working condition 1
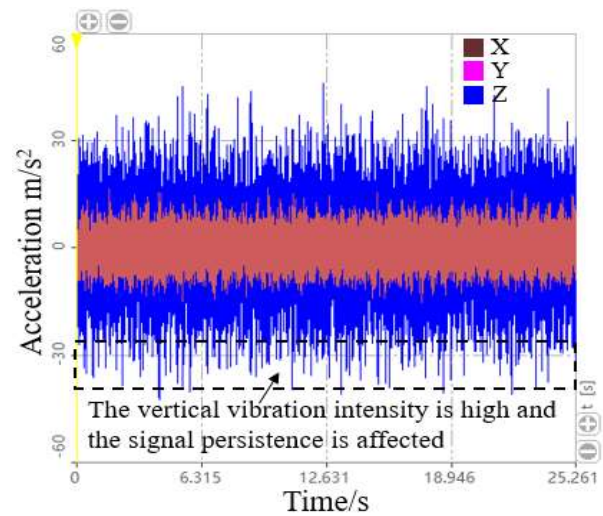


(b) Working condition 2

FIGURE 10. Time-domain signals at measuring point 7.

As can be seen from Figure 10, the time-domain response at measuring point 7 at the left front end of the chassis frame shows a similar characteristic trend to that at measuring point 8, at the rear end. The RMS values for the two measuring points in the Z-direction increase from 2.085 and 1.995 m/s$^2$ to 10.469 and 7.287 m/s$^2$, respectively. Hence, the phenomenon of significant longitudinal vibration of the frame during operation of the working parts is verified. Furthermore, a short-time Fourier transform (STFT) is applied to the signals in the direction of the maximum vibration intensity at each measuring point to obtain their frequency responses, and the results are shown in Figure 11.
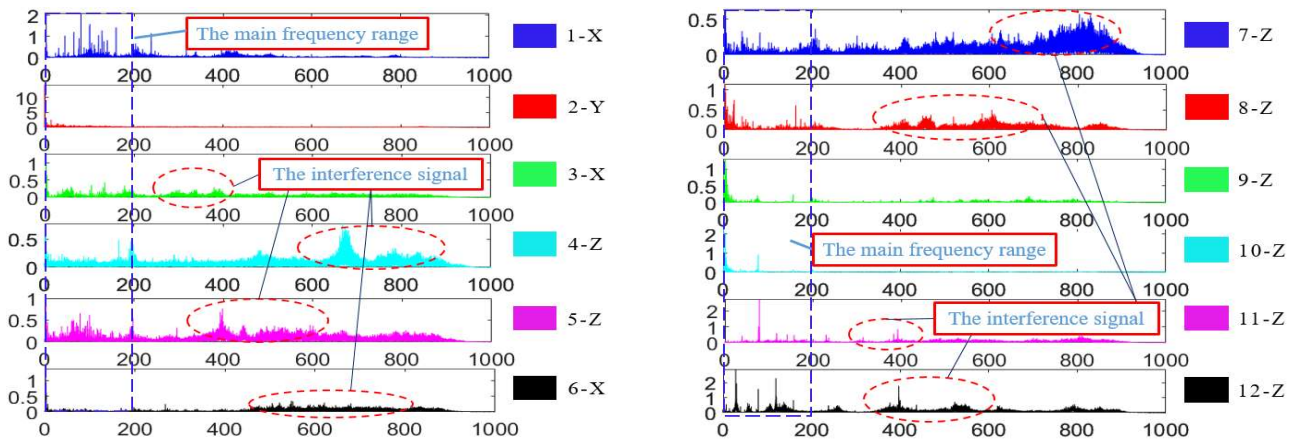
FIGURE 11. Main vibration direction spectrum at each measuring point.

From an analysis of the working parameters of the machine, it can be seen that the frequency response at each position is concentrated in the low-frequency band under normal operating conditions, although there are high-frequency components with wide bandwidth in many places in Figure 11. In particular, sidebands with high-frequency signals as the centre frequency appear at 4-Z, 7-Z, and 6-X. The sidebands at 3-X, 5-Z, 8-Z, and 12-Z are mainly centred on intermediate frequency components. In addition to the low-frequency effective signals, the other measuring points also have additional interference signals.

These random interference signals mainly arise from the resonance and friction caused by the movable connections between working parts and the frame, and therefore appear in the frequency spectrum as frequency signals with a wide bandwidth rather than several abrupt peaks.

Hence, according to the vibration energy intensity and frequency distribution of the above signals, only the low-frequency effective signals at the measuring points 1-X, 2-Y, 6-X, 7-Z, 8-Z, and 12-Z within the range 0–200 Hz are retained for analysis.
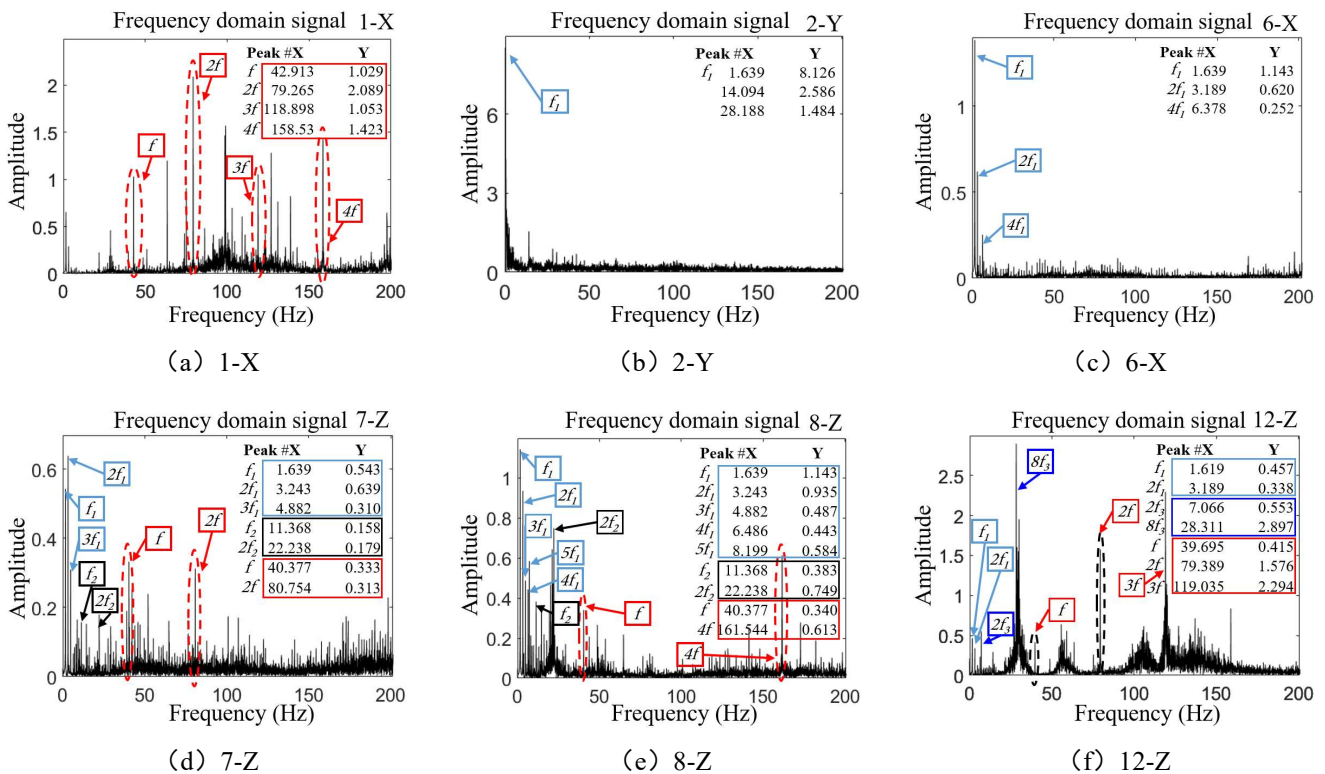


FIGURE 12. Low-frequency spectra.

The processed spectrum distribution diagrams are shown in Figure 12. The vibration frequency at the measuring point 1-X at the connection position of the engine rack includes the main frequency and multipliers of each order. Figure 12(c) shows the spectrum diagram for the low-frequency components at point 6-X. The rated operating speed of the drive shaft of the compression mechanism is around 96 r/min. It can be seen that the frequency components at this position are relatively simple, and the spectrum includes the main vibration frequency of the compression mechanism at 1.639 Hz and the double frequency at 3.189 Hz and quadruple frequency at 6.378 Hz. This frequency and its multipliers appear repeatedly in the main peak vibration frequencies for the remaining key working parts and the

positions of the response points. From the data for measuring points 7-Z, 8-Z, and 12-Z, it can be seen that the peak vibration of the frame is most obvious in the Z-direction, and most of the largest amplitudes are near a frequency of 1.6 Hz. The second highest vibrations are in the X-direction. In addition to the operating frequency of the compression mechanism, there are the same engine frequency as the measuring point 1-X and part of the excitation frequency of the engine drive shaft. This shows that the large longitudinal vibration amplitude of the frame is mainly caused by the periodic excitation force when the compression mechanism is working; it also indicates that the vibration caused by the reciprocating motion of the compression mechanism is second

only to the high-frequency vibration of the engine, which affects the response of the frame. The position near the centroid position of the machine body therefore presents periodic vibration.

We also considered the fact that the signals collected by the sensor during the test mostly contained high-frequency interference signals, and could not directly reflect the change in the frequency with time. We therefore used a low-pass filter to analyse the amplitude spectrum response in the X-direction at measuring point 8 of the chassis within 200 Hz under working condition 2. The power spectra for the vibration signal before and after filtering are shown in Figure 13.
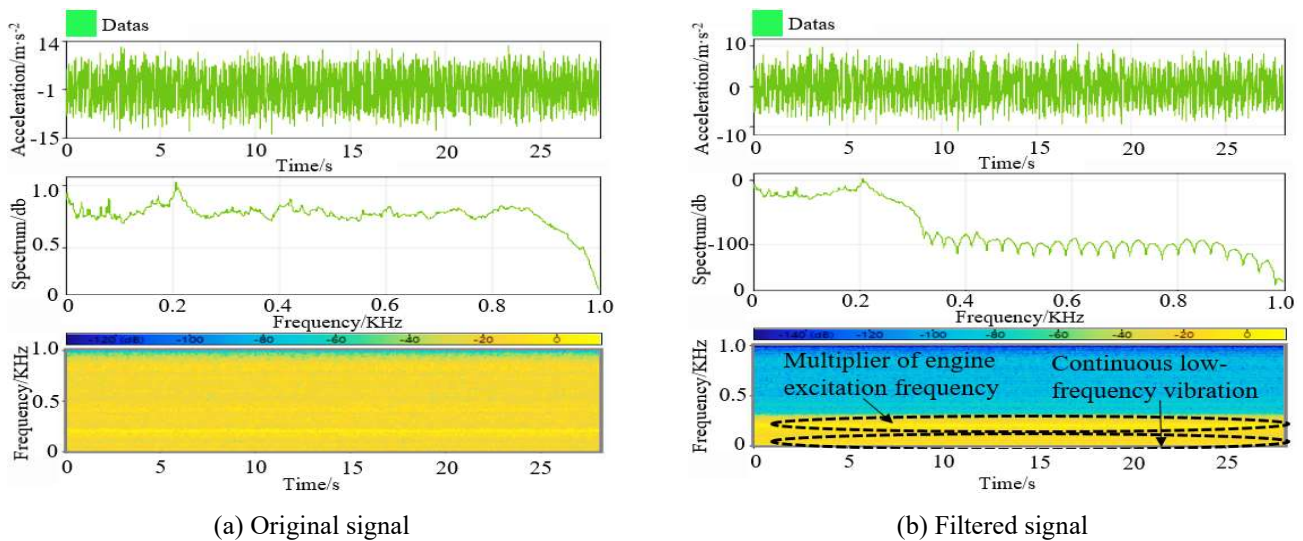


(a) Original signal

(b) Filtered signal

FIGURE 13. Comparison of spectra at measuring point 8, before and after filtering of the signal.

It can be seen from Figure 13(a) that there are strong vibration signals across the entire frequency band. After low-pass filtering, two prominent yellow lines can be observed in the time-frequency plot, and the peak frequency trajectories fluctuate smoothly around the two main response frequencies. This indicates that the engine excitation frequency and the low-frequency vibration of the compression mechanism have a sustained impact on the frame.

The vibration response characteristics of the machine body under running conditions were obtained through experiments under two different working conditions in an outdoor field. The response points were positioned on the top cover of the body, and were numbered 1 to 8 from front to back, with a spacing of 10 cm between adjacent measurement points. Positive and negative vibration amplitude data in three directions at each measurement point were obtained by calculation of the acceleration signals, as shown in Figure 14.



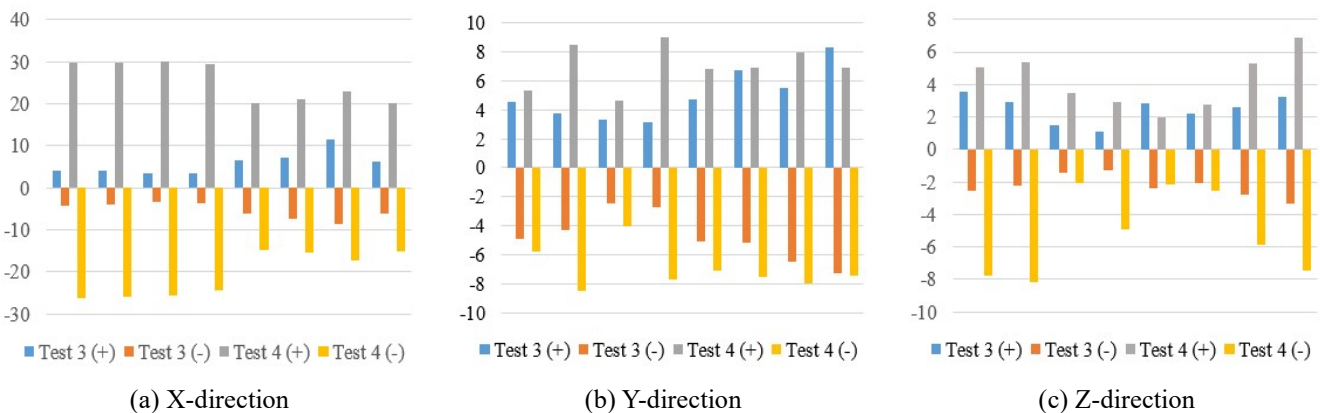(a) X-direction

(b) Y-direction

(c) Z-direction

FIGURE 14. Distributions of displacement data obtained from an outdoor test.

From the data, it can be seen that when the operating conditions for the machine body were changed from condition 3 to condition 4, the vibration amplitude in the X-direction at the measurement points changed the most. More specifically, the positive amplitude at the front (measurement point 1) increased from 4.186 to 29.871 mm. When the components were in operation, the vibration amplitude in the X-direction gradually decreased from measurement points 1 to 5 before gradually increasing again at point 7. The vibration amplitude in the Z-direction gradually decreased from measurement points 1 to 4 before gradually increasing again at point 8. This indicates that the position between measurement points 4 and 5 is continuously approaching the longitudinal centroid

position of the entire machine; the amplitude of longitudinal vibration at this position increased from 1.1 to 2.9 mm.

**Parameter analysis of multi-point motion**

The motion information at the unit points can be clearly obtained using ADAMS, as shown in Figure 15. The compression piston is driven by a constant speed crank, and its nearest and farthest points correspond to the highest and lowest points on the displacement curve. It can be found that the piston has a stroke of approximately 530 mm over one cycle of 0.62 s of reciprocating motion, which is close to the actual displacement. Hence, the accuracy of our kinematic model is validated.
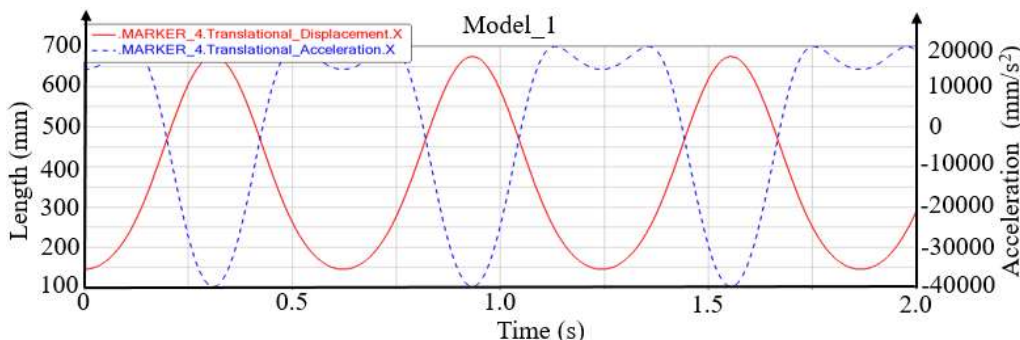


FIGURE 15. Graph of piston displacement and acceleration.

Under the no-load operating condition, it can be inferred from the position of the piston that the maximum acceleration magnitude is 39871.52 mm/s$^2$. Meanwhile, as shown in Figure 16(a), the force at the connection between the drive shaft and the gearbox gear changes rapidly under no-load operation, especially in the X- and Y-directions,

where the nonlinear time-varying excitation force is relatively large. The peak force magnitudes are 2980.85 and 1054.27 N, respectively. This also indicates that the vibration impact on the frame caused by excessive unbalanced inertia force during the no-load operation of the mechanism is significant.
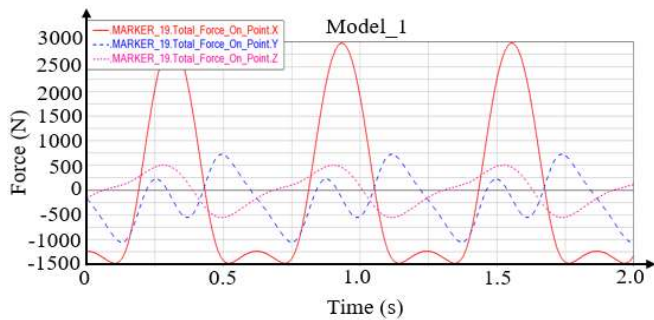


(a) No-load condition
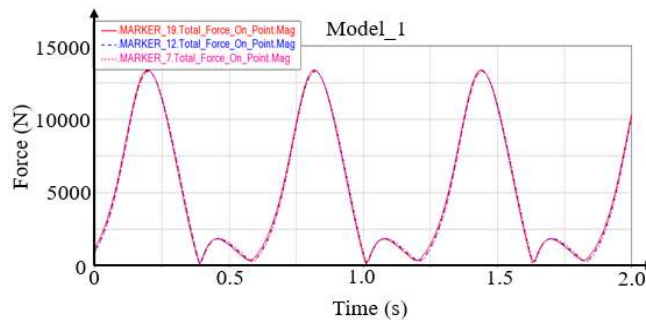


(b) Working conditions of straw compression

FIGURE 16. Force diagrams for the position of connection of the transmission shaft.

During the process of uniform feeding of straw, the trend in the combined forces acting on the three connection points is similar. As shown in Figure 16(b), at the beginning of the simulation, the piston is located at the initial position of motion; at this instant, the density of the straw is minimal and the volume of the compression chamber is at its maximum. The compressive force at each connection point of the mechanism increases continuously, and reaches a maximum at around 0.2 s, at which time the crank and connecting rod are at a 90º angle. At around 0.4 s in the simulation, the crank and connecting rod are at a 90º angle again, at which time the compression process of the mechanism is completed and the piston is in the process of returning. The force gradually decreases and a fluctuation

appears near the minimum value; then the force rises again at 0.58 s, entering a new compression operation process from 0.62 s. Finally, the maximum force data at each connection point in the simulation were obtained through the post-processing module. The maximum forces at the connection points between the crank and the output shaft of the gearbox, the crank and the connecting rod, and the connecting rod and the fixed axis hinge of the piston were found to 13367.01, 13296.88, and 13273.41 N, respectively.

**Comparison of results from simulation and tests**

A simulation model of the whole-machine vibration system was established in the MATLAB/Simulink dynamic system environment. The inputs at each excitation source

position were created by superimposing standard sine functions of different frequencies. The amplitude and period were obtained from the actual collected vibration signals, and the phase was set to zero. The vibration system model of the whole machine was established based on nine differential equations for the vibration of the frame and the vibration sources. Finally, the simulation results were analysed by outputting the signals through two modules to study the response characteristics of the chassis frame and the baling frame under excitation. The construction of the model is shown in Figure 17.
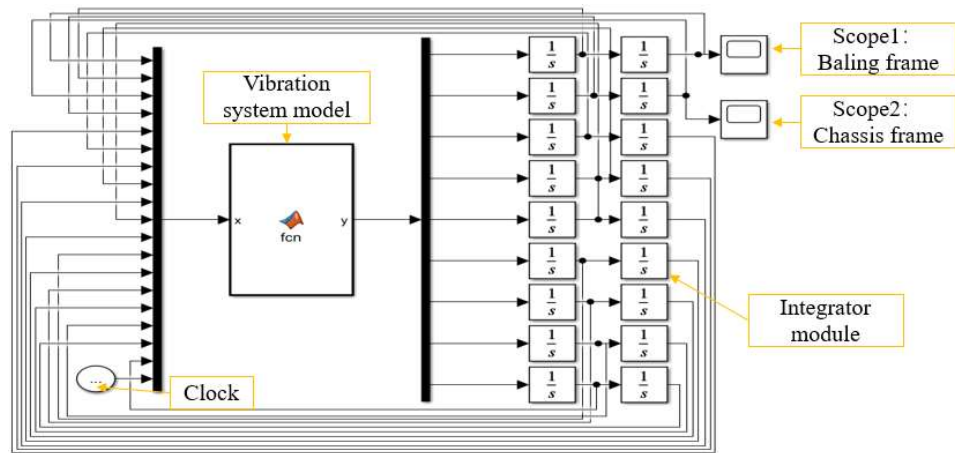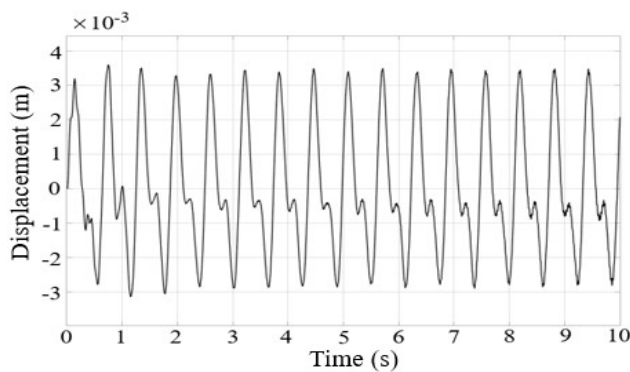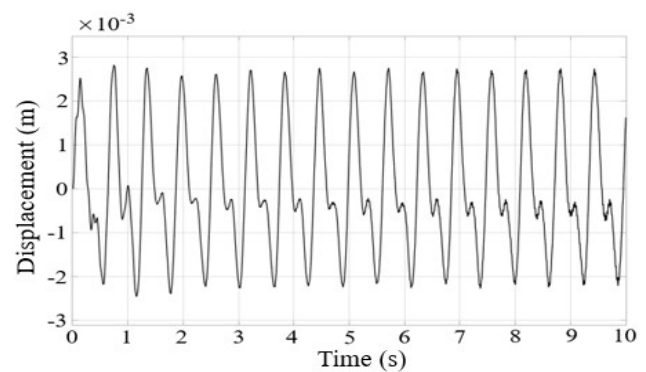


FIGURE 17. Simulink simulation model for the whole machine.

In this model, the simulation time was set to 10 s, the maximum simulation step was 0.001, and the other relevant simulation parameters in the model were also set. The ode45 solver was used for the calculations. Finally, the time-domain displacement change curves of the baling frame and the chassis frame in the vertical direction were obtained as shown in Figures 18(a) and (b), respectively.



(a) Chassis frame

(b) Baling frame

FIGURE 18. Results of the Simulink simulation.

It can be seen from the simulation results that the time-domain displacement curves for the frame show significant vibration and change periodically, with the waveform of the curves stabilizing after 1 s. Meanwhile, due to the small damping coefficient and very large stiffness coefficient between the baling frame and the chassis frame, the changes in the time-domain displacement curves for the two frames under excitation are consistent, although the peak value for the displacement curve of the baling frame is slightly larger. This is because the excitation of the working parts of the baling frame attenuates during transmission, a finding that is consistent with the previous analysis.

Furthermore, the signal amplitude of the stable displacement curve of the chassis frame centroid position increases from 1.79 to 2.82 mm during normal operation. The period of the displacement curve is consistent with the operation period of the compression mechanism at 0.62 s, which is consistent with the experimental results mentioned earlier. Hence, the accuracy of the dynamic simulation model is proved, and it is found that the unbalanced excitation force of the compression mechanism during the straw compression process will cause significant swinging in the longitudinal direction near the centroid position of the frame. This finding can provide a basis for further reducing the vibration amplitude of the frame and optimising the design of the frame in future work.

**CONCLUSIONS**

The aim of this paper was to determine the response characteristics of the longitudinal oscillation of a self-propelled baler around the centroid position of the frame undergoing excitation caused by straw compression. A suitable whole-machine dynamic model was established, and can provide a reference for further optimisation design to reduce the vibration amplitude of the machine body. The following conclusions can be drawn from this study:

(1) By analysing the vibration signals of the frame obtained under multiple on-site working conditions in the time-frequency domain and combing these with a power

spectrum analysis, the characteristic parameters of the no-load condition and the operation process were compared. The results indicate that the main response frequency of the frame during the straw compression operation is around 1.6 Hz, which is the working frequency of the compression mechanism. The amplitude of swinging near the centroid position of the frame under longitudinal excitation was also quantified.

(2) Through a multi-body dynamics simulation analysis in ADAMS, the changing trends of the force at different connection positions of the compression mechanism were compared, and the maximum force at the connection between the crank and the output shaft of the gearbox was obtained as 13367.01 N. The force at other positions decreased accordingly, indicating that the mechanism was subject to significant impact during the straw compression process.

(3) By establishing a nine-degree-of-freedom vibration system model of the entire machine, we characterised the vibration amplitude state of the machine body during the straw compression process. The simulated displacement curve of the chassis had a stable period of 0.62 s, which was consistent with the reciprocating motion period of the mechanism. The simulated displacement amplitude of the centroid position of the frame was found to consistent with experimental measurements, with a peak amplitude of about 3 mm, thus effectively verifying the effectiveness and accuracy of the dynamic model.

## REFERENCES

Albaghdadi AM, Baharom MB, Sulaiman SA (2021) Tri-planar balancing optimization of a double crank-rocker mechanism for shaking forces and shaking moments reduction. Proceedings of the Estonian Academy of Sciences 70(3): 286. https://doi.org/10.3176/proc.2021.3.07

Bai XW, Zhao P, Li YK, Liu J (2011) Modal analysis of a type of square baler's framework. Proceedings of 2011 International Conference on Electronic & Mechanical Engineering and Information Technology. IEEE 2011(4): 1769-1772. https://doi.org/10.1109/EMEIT.2011.6023445

El-Sayed SA, Elsaid Mohamed MK (2018) Mechanical properties and characteristics of wheat straw and pellets. Energy & Environment 29(7): 1224-1246. https://doi.org/10.1177/0958305X18772414

Etesami G, Felezi ME, Nariman-Zadeh N (2019) Pareto optimal multi-objective dynamical balancing of a slider-crank mechanism using differential evolution algorithm. International Journal of Automotive Engineering 9(3): 3021-3032. https://doi.org/10.22068/ijae.9.3.3021

Guerrieri AS, Anifantis AS, Santoro F (2019) Study of a large square baler with innovative technological systems that optimize the baling effectiveness. Agriculture 9(5): 86. https://doi.org/10.3390/agriculture9050086

Guo H, Gao GM, Zhou W, Liu JJ, Hao LJ (2022) Design of Load and Bale Density Monitoring and Control System for a Wheeled Self-Propelled Square Baler. Journal of the ASABE 65(3): 599-608. https://doi.org/10.13031/ja.14813

Han JW, Ding WX (2023) Research on vibration reduction based on lightweight design of sliding blocks. Forging technology 48(3). https://doi.org/10.13330/j.issn.1000-3940.2023.03.025

Khawaja AN, Khan ZM (2022) DEM study on threshing performance of "compression–oscillation" thresher. Computational Particle Mechanics 9: 1233-1248. https://doi.org/10.1007/s40571-021-00456-4

Langer TH, Ebbesen MK, Kordestani A (2015) Experimental analysis of occupational whole-body vibration exposure of agricultural tractor with large square baler. International Journal of Industrial Ergonomics 47: 79-83. https://doi.org/10.1016/j.ergon.2015.02.009

Li YM, Zhu LH, Tang Z, Xu LZ (2017) Finite element modal analysis and experiment of the compression device of the all-in-one machine of combine harvester and baler. 2016 International Forum on Mechanical, Control and Automation (IFMCA 2016). Atlantis Press 2017: 510-519. https://doi.org/10.2991/ifmca-16.2017.78

Liu HY, Gao N, Meng ZJ, Zhang AQ, Wen CK, Li HQ, Zhang J (2023) Construction and test of baler feed rate detection model based on power monitoring. Agronomy 13(2): 425. https://doi.org/10.3390/agronomy13020425

Ma Z, Zhang ZL, Zhang ZH, Song ZQ, Liu YB, Li YM, Xu LZ (2023) Durable Testing and Analysis of a Cleaning Sieve Based on Vibration and Strain Signals. Agriculture 13(12): 2232. https://doi.org/10.3390/agriculture13122232

Pang J, Li YM, Ji J, Xu LZ (2019) Vibration excitation identification and control of the cutter of a combine harvester using triaxial accelerometers and partial coherence sorting. Biosystems Engineering 185: 25-34. https://doi.org/10.1016/j.biosystemseng.2019.02.013

Shi Y, Jiang Y, Wang X, Thuy NTD, Yu H (2023) A mechanical model of single wheat straw with failure characteristics based on discrete element method. Biosystems Engineering 230: 1-15. https://doi.org/10.1016/j.biosystemseng.2023.03.017

Song DQ, Wang G, Xue Z, Zhang J, Huang ZM, Yang ZZ (2014) Design and analysis on compression mechanism of small square bales of sugarcane leaf baler. Agriculture engineering & Agriculture machinery 15(10): 1812-1815. https://doi.org/10.16175/j.cnki.1009-4229.2014.10.097

Tang HZ, Chen XS, Xue ZY, Xing XM, Li MW, Lv GD, Guo HJ (2020a) Development of intelligent rice-wheat combine harvesting and baling machine. Conference Series 1635(1): 012068. https://doi.org/10.1088/1742-6596/1635/1/012068

Tang H, Xu WL, Zhao JL, Xu CS, Wang JW (2023) Comparison of rice straw compression characteristics in vibration mode based on discrete element method. Biosystems Engineering 230: 191-204. https://doi.org/10.1016/j.biosystemseng.2023.04.009

Tang Z, Zhang B, Liu X, Ren H, Li XY, Li YM (2020b) Structural model and bundling capacity of crawler picking and baling machine for straw wasted in field. Computers and Electronics in Agriculture 175: 105622. https://doi.org/10.1016/j.compag.2020.105622

Tao L, Wang YJ, Liu GY, Zhen JQ, Yang HY (2017) Lightweight frame design of straw baler. Journal of Chinese Agricultural Mechanization 38(8): 26-33. https://doi.org/10.13733/j.jcam.issn.2095-5553.2017.08.006

Wang CN, Le TDM, Huynh NT (2023) Optimal rigid-flexible dynamic of space slider-crank mechanism with clearance joints. Sādhanā 48(2): 44. https://doi.org/10.1007/s12046-023-02085-4

Wang QQ, Bai ZW, Li ZQ, Xie DB, Chen LQ, Wang H (2021) Straw/spring teeth interaction analysis of baler picker in smart agriculture via an ADAMS-DEM coupled simulation method. Machines 9(11): 296. https://doi.org/10.3390/machines9110296

Wei CC, Xu LZ, Wang JT, Li YM (2018) Inertial force balance and ADAMS simulation of the oscillating sieve and return pan of a rice combine harvester. International Journal of Agricultural and Biological Engineering 11(1): 129-137. https://doi.org/10.25165/j.ijabe.20181101.2978

Xu LZ, Chai XY, Gao ZP, Li YM, Wang YD (2019) Experimental study on driver seat vibration characteristics of crawler-type combine harvester. International Journal of Agricultural and Biological Engineering 12(2): 90-97. https://doi.org/10.25165/j.ijabe.20191202.3657

Yin JJ, Chen ZJ, Liu C, Zhou ML, Liu L (2023) Design and Experiments of a Real-Time Bale Density Monitoring System Based on Dynamic Weighing. Sensors 23(4): 1778. https://doi.org/10.3390/s23041778

Yu ZW, Li YM, Xu LZ, Du XX, Ji KZ (2024) Unbalanced variation after assembly and double-speed influence coefficient method in the threshing drum. International Journal of Agricultural and Biological Engineering 16(6): 1-10. https://doi.org/10.25165/j.ijabe.20231606.7651

Zhang XL, Peng KD (2018) Vibration control method for a crawler-type combine harvester. Emirates Journal of Food and Agriculture 30(10): 873-882. https://doi.org/10.9755/ejfa.2018.v30.i10.1831

Zhao Z, Huang HD, Yin JJ, Yang SX (2018) Dynamic analysis and reliability design of round baler feeding device for rice straw harvest. Biosystems Engineering 174: 10-19. https://doi.org/10.1016/j.biosystemseng.2018.06.014